



Stiff, porous scaffolds from magnetized alumina particles aligned by magnetic freeze casting



Michael B. Frank^{a,*}, Steven E. Naleway^b, Tsuk Haroush^c, Chin-Hung Liu^a, Sze Hei Siu^c, Jerry Ng^c, Ivan Torres^c, Ali Ismail^c, Keyur Karandikar^a, Michael M. Porter^d, Olivia A. Graeve^{a,c}, Joanna McKittrick^{a,c}

^a Materials Science and Engineering Program, University of California, San Diego, 9500 Gilman Drive, La Jolla, CA 92093, USA

^b Department of Mechanical Engineering, University of Utah, 1495 E 100 S, Salt Lake City, UT 84112, USA

^c Department of Mechanical and Aerospace Engineering, University of California, San Diego, 9500 Gilman Drive, La Jolla, CA 92093, USA

^d Department of Mechanical Engineering, Clemson University, Clemson, SC 29634, USA

ARTICLE INFO

Article history:

Received 24 September 2016

Received in revised form 5 January 2017

Accepted 25 March 2017

Available online 29 March 2017

Keywords:

Freeze casting

Ferrofluid

Magnetic alignment

Ceramic scaffold

Mechanical properties

ABSTRACT

Bone consists of a hard mineral phase and a compliant biopolymer phase resulting in a composite material that is both lightweight and strong. Osteoporosis that degrades spongy bone preferentially over time leads to bone brittleness in the elderly. A porous ceramic material that can mimic spongy bone for a one-time implant provides a potential solution for the future needs of an aging population. Scaffolds made by magnetic freeze casting resemble the aligned porosity of spongy bone. A magnetic field applied throughout freezing induces particle chaining and alignment of lamellae structures between growing ice crystals. After freeze drying to extract the ice and sintering to strengthen the scaffold, cubes from the scaffold center are mechanically compressed along longitudinal (*z*-axis, ice growth direction) and transverse (*y*-axis, magnetic field direction) axes. The best alignment of lamellar walls in the scaffold center occurs when applying magnetic freeze casting with the largest particles (350 nm) at an intermediate magnetic field strength (75 mT), which also agrees with stiffness enhancement results in both *z* and *y*-axes. Magnetic moments of different sized magnetized alumina particles help determine the ideal magnetic field strength needed to induce alignment in the scaffold center rather than just at the poles.

© 2017 Elsevier B.V. All rights reserved.

1. Introduction

Gravity and electromagnetism are natural forces responsible for celestial body assembly in the universe. Earth's magnetic field plays a role in "biological body" assembly, or how living organisms orient themselves with respect to their surrounding environment [1]. Biogenic magnetite (Fe_3O_4) has been found in sharks [2], pigeons [3], honeybees [4], humans [5], and most notably in magnetotactic bacteria that align parallel to the earth's magnetic field direction in search of microaerophilic regions of low oxygen concentration [6]. These bacteria have single domain Fe_3O_4 crystals packaged within organelle magnetosomes that form a chain along the long axis of the bacteria. Magnetosome alignment within these bacteria provides an interesting avenue for bioinspired applications that use aligned materials to resemble naturally ordered structures.

Strong magnetic fields (≈ 9 –18 T) have been used along with a slip casting process to finely control and texture anisotropic ceramic particles to improve their physical, chemical and mechanical properties [7–15]. Macroscopic alignment occurs when the magnetic energy on

rotation exceeds the thermal energy for the slurry particles. In addition to the strong magnetic field, the degree of particle orientation depends on several processing factors, such as heating temperature, particle size and suspension viscosity [10]. Magnetic slip casting used at much lower magnetic field strength (< 40 mT) can also be used to manipulate surface magnetized alumina (Al_2O_3) platelets [16]. Fine control over these materials has led to reinforced composites [17–20], self-shaping composites [21], tunable fluorescence emission [22], and additive manufacturing processes such as 3D magnetic printing [23,24].

Bone consists of nanomaterials (grains, platelets or fibers) organized into a hierarchical structure that form a composite with high strength and toughness [25]. It must be strong to support the body, tough to absorb impact forces, lightweight to enable movement, and porous to replenish nutrients [26,27]. Cortical bone provides a dense outer sheath while the inner trabecular bone enables marrow production and cell growth within the large interconnected pores of the spongy bone interior [27]. Pore alignment in load bearing regions is an important design feature along with prevention of pore expansion due to osteoporosis [28]. Fabrication of aligned porous structures that resemble trabecular bone necessitates methods that can provide dual levels of control over structural features with disparate length scales and along multiple directions.

* Corresponding author.

E-mail address: mbfrank@ucsd.edu (M.B. Frank).

Freeze casting is a physical process that uses an aqueous slurry consisting of a particulate solid phase (e.g., ceramic particles) and a freezing agent (e.g., water) to fabricate a porous scaffold [29–33]. First, ice templated crystal growth separates particles into lamellar structures aligned along the freezing direction (*z*-axis). Following freeze drying and sintering steps to remove ice crystals and strengthen the overall macrostructure, respectively, the resulting porous scaffold has lamellar walls interconnected by mineral bridges. The quantity and dimension of the pores can be modified by adjusting the solid loading [34,35], changing the liquid freezing agent [36–38], and introducing additives [39–43]. Alumina has often been used for the solid particles in prior freeze casting work that varied experimental parameters and characterization techniques [43–46]. Although scaffolds are typically strong in the ice growth direction, mechanical properties in transverse directions (*x*, *y*-axes) normal to the freezing direction are generally poor due to non-aligned lamellar walls.

Various techniques for transverse lamellar alignment within freeze cast scaffolds exist [47–50], however, Porter, et al. were first to apply a magnetic field during freeze casting for that purpose [51]. When subjected to a transverse magnetic field (≈ 120 mT, *y*-axis) normal to the ice growth direction (*z*-axis), a slurry of paramagnetic titania (TiO₂, 200–500 nm) and ferromagnetic Fe₃O₄ (≈ 50 nm) aligned lamellar walls to make mechanically enhanced scaffolds. Magnetic freeze casting with a slurry of diamagnetic zirconia (ZrO₂, 200–500 nm) and Fe₃O₄ in a rotating magnetic field (≈ 120 mT) made torsion enhanced helical banded scaffolds [52], while a transverse magnetic field (≈ 90 mT) made scaffolds with bridge-like features [53]. Distinct phase separation occurred with ZrO₂, but not with TiO₂, which was due to lack of interparticle interaction with Fe₃O₄ when subjected to the applied magnetic field.

Superparamagnetism occurs in smaller Fe₃O₄ particles (<15–20 nm) as a super moment that can easily flip in response to a changing magnetic field when the particle thermal energy ($k_B T$, Boltzmann's constant \cdot temperature) exceeds the magnetic anisotropy energy barrier ($K_{eff} V$, anisotropy constant \cdot particle volume) [54]. Dynabeads® (Thermo Fisher Scientific, Waltham, MA) use a superparamagnetic Fe₃O₄ particle core and functionalized polystyrene shell for magnetic separation applications [55]. An alternative surface magnetization method uses an aqueous suspension of dispersed superparamagnetic Fe₃O₄ (ferrofluid) coated with charged surfactant that can electrostatically adsorb onto particles. This method uses the point-of-zero charge (PZC), the pH when particles become electrostatically neutral in water [56], and the hydroxylated surface is protonated or deprotonated according to Gouy-Chapman theory [57]. Since Al₂O₃ (PZC ≈ 9) [58] in water (PZC ≈ 7) is protonated, anionic charged Fe₃O₄ can surface magnetize Al₂O₃ particles through electrostatic adsorption.

Equations that describe chain formation of single domain Fe₃O₄ (≈ 50 nm) in magnetosomes of magnetotactic bacteria [59] can be used to predict how isolated superparamagnetic Fe₃O₄ particles [60] and Dynabeads® [61,62] in water respond to a magnetic field gradient. The maximum value of the magnetic interaction energy (U^*) is indicated in Eq. (1)

$$U^* = \frac{\mu_0 m^2}{2\pi d^3} \quad (1)$$

where μ_0 is the magnetic permeability of free space ($4\pi \times 10^{-7}$ H/m), m is the particle magnetic moment dipole and d is the center-center interparticle distance (equal to one particle diameter for particles touching in a chain) [63]. The ratio between U^* and thermal energy ($k_B T$) is the magnetic coupling parameter (Γ) indicated in Eq. (2) (Supplementary Fig. 1).

$$\Gamma = \frac{U^*}{k_B T} = \frac{\mu_0 m^2}{2\pi d^3 k_B T} \quad (2)$$

However, a value of $\Gamma > 1$ by itself does not account for thermodynamic considerations due to loss of entropy associated with chain formation. The solution conditions responsible for the balance between energy and entropy are incorporated in the aggregation parameter (N^*) indicated in Eq. (3)

$$N^* = \sqrt{\phi_0 e^{\Gamma-1}} \quad (3)$$

where ϕ_0 is the volume fraction (vol%) of the slurry. For example, a 10 vol% slurry necessitates $\Gamma > 3.31$ to get chain formation at $N^* > 1$. For magnetic freeze casting, where particle self-assembly into chains is desirable for fabricating aligned lamellar structures, Eq. (3) provides a valuable predictive tool based on measurable parameters that mechanical characterization of sintered scaffolds can further validate.

This work investigates a new method for making multi-axis strengthened porous structures that resemble trabecular bone by magnetic freeze casting with surface magnetized Al₂O₃ particles. Magnetic control over superparamagnetic Fe₃O₄ electrostatically adsorbed to Al₂O₃ particles leads to lamellar wall alignment and stiffness enhancement in the transverse direction. Structural materials typically used for freeze casting that are either paramagnetic (e.g., TiO₂) or diamagnetic (e.g., ZrO₂, Al₂O₃, hydroxyapatite) can become magnetically responsive at low magnetic field strength. Thus, macro and microstructural feature control by magnetic freeze casting can provide a feasible fabrication pathway towards dynamic material systems that sense, interact with and even adapt to the surrounding environment [64].

2. Materials and methods

2.1. Particle surface magnetization

Three different α -Al₂O₃ particles (BMA15, 150 nm; SM8, 350 nm; CR6, 500 nm; bulk density of 3960 kg/cm³ [65]; particle size estimated by supplier Baikowski, Malakoff, TX, USA) were surface magnetized (Supplementary Fig. 2). For each particle size, 2.5 g Al₂O₃ was stirred in 75 mL distilled water, while 100 μ L of anionic ferrofluid (EMG-705, 1–4 vol% Fe₃O₄ nanoparticles, Ferrotec, Bedford, NH, USA) was diluted in 5 mL distilled water in a separate container and dropwise added to the stirring Al₂O₃ solution at 700–800 rpm (RO 15 P S1, IKA Works, Wilmington, DE, USA). After stirring for 12 h, white colored Al₂O₃ particles changed to a light brown color and the surrounding solution became clear. Residual anionic surfactant was rinsed off from magnetized particles with distilled water and vacuum filtration. The magnetized Al₂O₃ was then dried for 12 h at 100 °C before use in magnetic freeze casting slurries.

2.2. Magnetic materials characterization

Magnetized Al₂O₃ particles (≈ 15 –30 mg) were characterized with a vibrating sample magnetometer (VSM, VersaLab, Quantum Design International, San Diego, CA, USA) with moment measured in response to a sweeping magnetic field (0–3000 Oe). Mass magnetization (M , emu/g) and particle magnetic moment (m , Am²) were calculated from magnetometer measurements coupled with particle volume (v) measured by the dynamic light scattering (DLS) technique, using Eqs. (4) and (5):

$$M = \text{moment/sample weight} \quad (4)$$

$$m = v \times M \quad (5)$$

2.3. Magnetized slurry preparation

Magnetized Al₂O₃ particle slurries (10 vol%) were prepared (by weight Al₂O₃) with polymer binders 1 wt% polyvinyl alcohol (PVA,

100,000 g/mol molecular weight (MW), Alfa Aesar, Ward Hill, MA, USA), 1 wt% polyethylene glycol (PEG, 10,000 g/mol MW, Alfa Aesar, Ward Hill, MA, USA) and 1 wt% anionic dispersant (Darvan 811, R. T. Vanderbilt Company, Inc., Norwalk, CT, USA). Al_2O_3 grinding media was added to the slurry and the mixture was ball milled for 24 h. After milling, particle sizes measured at least twenty times by DLS (Microtrac Nanotrak Wave II, Montgomeryville, PA) provided a number distribution of the mean particle diameter [66–68].

2.4. Magnetic freeze casting

A vise grip (Panavise, Reno, NV) with ≈ 420 mT bar magnets (N52 grade, K&J Magnetics, Inc. Pipersville, PA, USA) attached to either end allowed for a static magnetic field apparatus that was adjustable. A handheld Gauss meter measured the magnetic field strength at the gap, located at the midpoint between the magnets. An exponential curve fit from the data points was acquired at successively increasing 5 mm gap intervals, yielding an equation for conversion of gap distance to magnetic field strength. The Gauss meter measurements closely resembled calculated values for two disc magnets attached to an iron yoke (Supplementary Fig. 3). Freeze casting with magnetized Al_2O_3 subjected to no magnetic field versus a static transverse magnetic field ($\approx 25, 75, 150$ mT) was accomplished in a polyvinyl chloride (PVC) mold. A groove was filed along the inside wall of the mold and aligned perpendicular to the magnetic field axis to provide a visual indicator where the magnetic field was applied on the sintered samples.

Each surface magnetized Al_2O_3 slurry was degassed under low vacuum for 15 min before pouring 5 mL into the PVC freeze cast mold. The static magnetic field apparatus was situated and centered over the PVC mold (Supplementary Fig. 4). Directional freezing occurred from the bottom upward using a custom built freeze casting device, as previously described [51]. Frozen solid samples were lyophilized with a bench-top freeze dryer (Labconco, Kansas City, MO, USA) at -50°C and 3.5×10^{-6} Pa for 48 h. Ice crystals sublimed leaving behind fragile ‘green body’ scaffolds composed of particles held together by the polymer binders. Samples were sintered in an open air furnace for 3 h at 1500°C with heating and cooling rates of $2^\circ\text{C}/\text{min}$, following a procedure that provided reproducible results with uniform porosity [51].

2.5. Mechanical characterization

A total of six scaffolds were prepared for each condition with Al_2O_3 particle size (195, 225, 350 nm) and magnetic field strength (75, 150 mT) as variables. Compression testing of sintered Al_2O_3 scaffolds was performed on a 3342 Instron materials testing machine (Instron, Norwood, MA) with a 500 N static load cell at a crosshead velocity of 0.005 mm/s following previous procedures [41,42,51,53]. Two samples ($\approx 5\text{ mm}^3$ cubes) cut from each scaffold center (Fig. 1) were compressed, one in the ice growth direction (z-axis) and the other in the magnetic field direction (y-axis). Ultimate compressive strength and Young's modulus were determined from the maximum stress and linear slope of the stress–strain curves, respectively.

2.6. Scanning electron microscopy characterization

Two of the six sintered scaffolds for each condition were sectioned at midpoint height, mounted to a stage and coated with colloidal graphite along the bottom and side walls. Iridium was sputter coated (EMITech K575X, Quorum Technologies Ltd., West Sussex, UK) for 15 s at 85 mA onto the top. Scanning electron microscopy (SEM) micrographs at 10 kV (spot size 3 nm) from a Philips XL30 field emission environmental scanning electron microscope (FEI-XL30, FEI Company, Hillsboro, OR) were used to characterize scaffold pore dimensions and look for general trends in lamellar wall alignment (horizontal, angled, none). Image analysis with ImageJ software (National Institutes of Health, Bethesda, MD, USA) maintained a contrast threshold at a consistent value in all

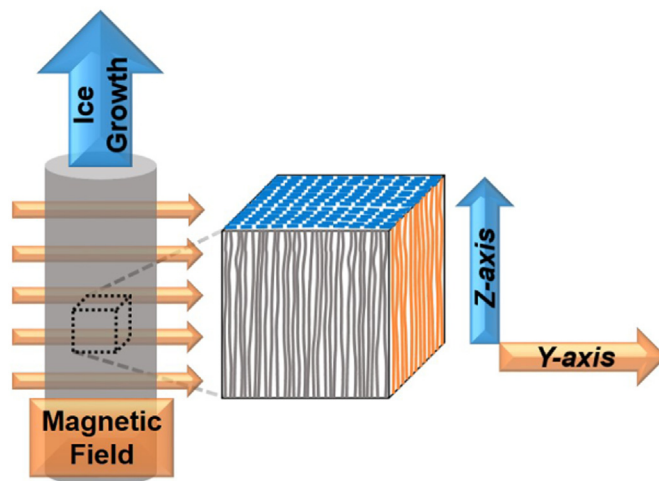


Fig. 1. Sintered scaffold cube compression diagram. Mechanical properties are compared via cubes from the center of the sintered scaffold compressed in the ice growth direction (z-axis, blue cube face) and the magnetic field direction (y-axis, orange cube face). (For interpretation of the references to color in this figure legend, the reader is referred to the web version of this article.)

micrographs. An ellipse fit to each measured pore provided dimensions for the major axis (a) and minor axis (b). For each scaffold, 40 individual pores were measured to obtain pore area ($A_p = \pi ab / 4$) and lamellar wall thickness (t), which was how other scaffolds were analyzed in previous work [41,42].

3. Results and discussion

3.1. Magnetic response of magnetized alumina particles

M - H curves from VSM measurements for surface magnetized Al_2O_3 particles (Supplementary Fig. 5) subjected to a sweeping magnetic field, H , and plotted versus M (emu/g, Eq. (4)) indicated an absence of hysteresis and magnetization at $H = 0$. These results support the applicability of Eqs. (1)–(3) from Faruqi, et al. [63] for chaining of composite superparamagnetic colloids. Interactions between surface adsorbed 10 nm Fe_3O_4 on neighboring Al_2O_3 particles that might have affected overall superparamagnetic properties were not observed. M - H curve values for susceptibility (maximum slope) and saturation (maximum mass magnetization) from surface magnetized Al_2O_3 were lessened compared with superparamagnetic Fe_3O_4 nanoparticles alone [69], but resembled values for composites with superparamagnetic Fe_3O_4 cores [70]. Additional VSM measurement of 50 nm Fe_3O_4 not used in this work confirmed the presence of hysteresis and magnetization at $H = 0$ for single domain, ferromagnetic nanoparticles that are not superparamagnetic (Supplementary Fig. 5).

Al_2O_3 particle sizes were estimated by the supplier to be 150 nm (BMA15), 300 nm (SM8) and 500 nm (CR6), however, average particle sizes measured by DLS after ball milling were actually 195 nm, 225 nm and 350 nm, respectively (Fig. 2). Since Al_2O_3 particles (195, 225, 350 nm) with equal mass (2.5 g) and density ($3.96\text{ g}/\text{cm}^3$) were surface magnetized with equal ferrofluid volume (0.1 mL), adsorbed amount of Fe_3O_4 nanoparticles (10 nm) onto each Al_2O_3 particle could be estimated with assumptions for spherical particle shape and Fe_3O_4 fraction in ferrofluid (4 vol%). Individual 195, 225 and 350 nm Al_2O_3 particles had an estimated 47, 72 and 272 adsorbed Fe_3O_4 nanoparticles, respectively.

Comparison between Al_2O_3 particle sizes demonstrated that 195 and 225 nm particles had $\approx 1.9\times$ and $\approx 1.7\times$ greater M values, respectively, than 350 nm particles (Fig. 3). Surface area to volume ratios for 195 nm and 225 nm particles were similarly $\approx 1.8\times$ and $\approx 1.6\times$ times greater, respectively, than for 350 nm particles. Multiplying M by mass of an

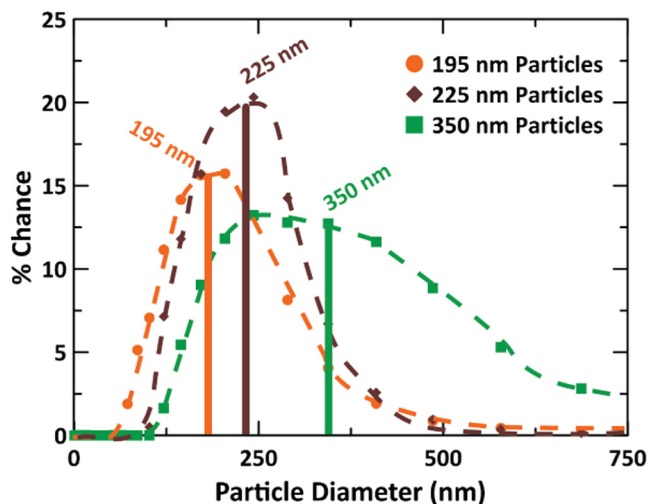


Fig. 2. Dynamic light scattering measurement of alumina particle sizes. Each particle type was segmented into a mean number distribution that consisted of particle percentage at different particle size bins and plotted for comparison. The product of each particle percentage with corresponding bin size was summed to determine the reported mean for each particle type.

individual Al_2O_3 particle (195, 225, 350 nm plus adsorbed Fe_3O_4 (47, 72, 272 nanoparticles, respectively) yielded magnetization values of 6.83×10^{-15} , 9.46×10^{-15} and 1.97×10^{-14} emu for surface magnetized 195, 225 and 350 nm Al_2O_3 , respectively, at 75 mT magnetic field strength. The magnetization per particle value for surface magnetized 350 nm Al_2O_3 was $\approx 2.1 \times$ and $\approx 2.9 \times$ greater than for 195 and 225 nm Al_2O_3 , respectively, which mirrored m values (Am^2 , Eq. (5)) for each composite particle size at varying magnetic field strength. Since Γ is proportional to m^2 (Eq. (2)), larger particles were more likely to overcome thermal agitation dominance and Brownian motion compared with smaller particles [61].

DLS measured average Al_2O_3 particle size, d , and VSM measured moment, m , were combined in Eq. (2) to obtain Γ as a function of applied magnetic field strength (left side, Fig. 4a–c). For each average particle size, Γ fell below the threshold for dipole-dipole interaction dominance when magnetic interaction energy exceeds thermal agitation ($\Gamma > 1$) as well as the threshold for particle chain formation when $N^* > 1$ for a

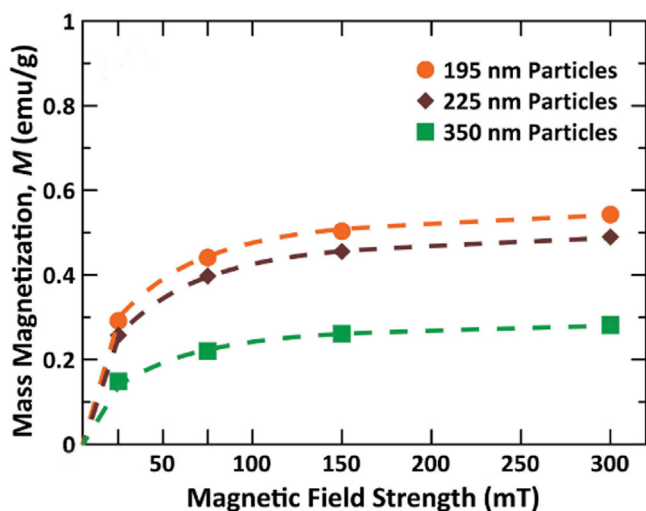


Fig. 3. Comparison of mass magnetization, M , determined from magnetometer measurements for different sized magnetized alumina particles. The value M is the measured magnetic moment divided by the sample weight. Greater surface area to volume ratio for smaller particles leads to greater values for M at various magnetic field strengths.

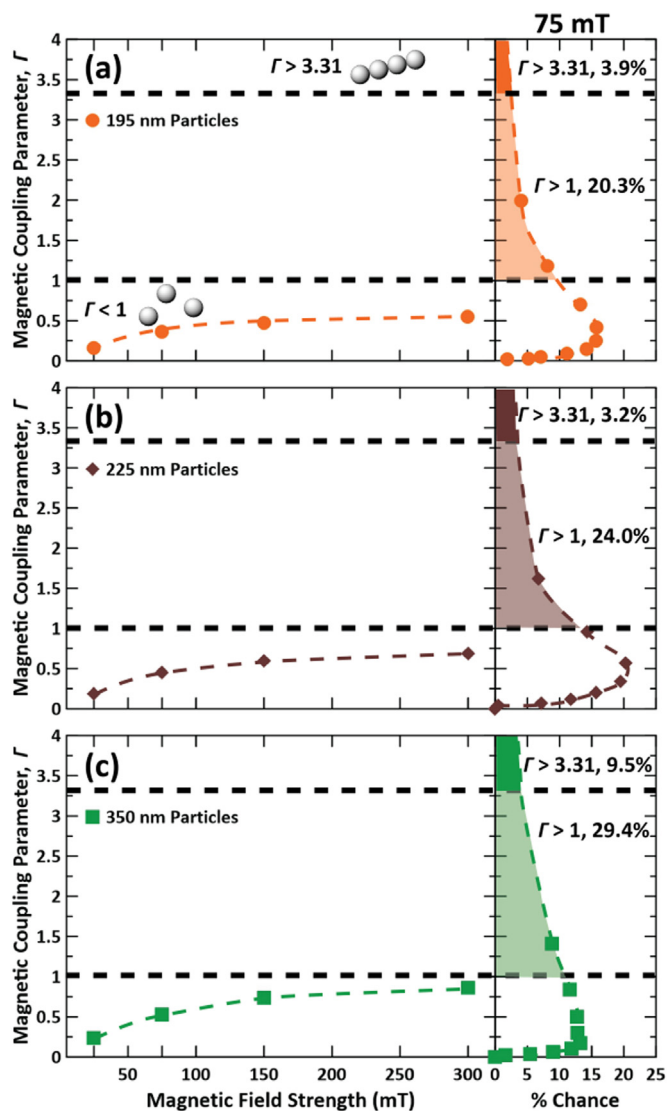


Fig. 4. Comparison of calculated magnetic coupling parameter (Γ) values and mean number distribution of particle sizes for different sized alumina particles. Average particle sizes for (a) 195 nm, (b) 225 nm and (c) 350 nm particles did not exceed $\Gamma > 1$ or $\Gamma > 3.31$ thresholds at any magnetic field strength. Mean number distribution measurements for particle sizes indicated a higher percentage of larger particles (350 nm) exceeded $\Gamma > 1$ and $\Gamma > 3.31$ thresholds at 75 mT.

10 vol% slurry ($\Gamma > 3.31$). Since average particle size poorly represents the actual size disparity evident in a mean number distribution for each Al_2O_3 particle type (Fig. 2), Γ was calculated at each DLS measured particle size by percent chance within the overall slurry. The percentage of each particle type above $\Gamma > 1$ and $\Gamma > 3.31$ thresholds at a magnetic field strength of 75 mT is indicated (right side, Fig. 4a–c). The 195, 225 and 350 nm particles had 20.3%, 24.0% and 29.4% of each type above $\Gamma > 1$, respectively, while 3.9%, 3.2% and 9.5% were above $\Gamma > 3.31$, respectively. Meanwhile at 150 mT, the 195, 225 and 350 nm particles had 26.9%, 34.3% and 37.4% of each type above $\Gamma > 1$, respectively, while 6.0%, 5.1% and 12.9% were above $\Gamma > 3.31$, respectively.

3.2. Lamellar wall alignment

During the time before freezing started, larger magnetized particles subjected to an applied magnetic field likely aggregated in a manner similar to previously reported 1D chain formation of Fe_3O_4 nanoclusters at room temperature in aqueous solution [71]. Additional experiments confirmed ice nucleation and crystal growth initiated at 247 K in freeze

cast slurries, thus that temperature value was used in Eq. (2) to calculate Γ values (Fig. 4). As slurry temperature decreased steadily (-10 K/min) from 283 K to 103 K during freeze casting, the applied magnetic field increased interaction energy between magnetized Al_2O_3 particles within the supercooled slurry for 3–4 min until ice growth started at 247 K. The percentage of larger slurry particles with enhanced interaction energy above $\Gamma > 1$ and $\Gamma > 3.31$ likely guided the formation of lamellar walls aligned along magnetic field lines between growing ice crystals. Mineral bridges made up of particles trapped within the growing ice front connected between adjacent lamellae in a similar fashion as in normal freeze casting.

In Fig. 5, SEM micrographs from the center of the scaffolds show transverse cross-sections perpendicular to the ice growth direction (Fig. 5a–c). No lamellar wall alignment occurred during freeze casting when there was no applied magnetic field. All the magnetic field conditions for 195 nm scaffolds had no lamellar wall alignment along the magnetic field axis (Fig. 5a). Some aligned regions were evident for 225 nm scaffolds at 150 mT, but not at lower strength magnetic fields

(Fig. 5b). For 350 nm scaffolds (Fig. 5c), more horizontal lamellar wall alignment occurred at 75 mT (Fig. 5d) than at 150 mT (Fig. 5e). High magnification SEM micrographs of 350 nm scaffolds showed horizontally aligned lamellar walls at 75 mT (Fig. 5f, g) along the magnetic field axis.

Image analysis of stitched together SEM micrographs (6 mm \times 2.7 mm) from the center of 350 nm scaffolds indicated $\approx 20\%$ horizontal lamellar wall alignment at 75 mT and $\approx 12\%$ horizontal alignment at 150 mT (results not shown). Among the scaffolds analyzed for each condition, a generally observed trend from SEM micrographs was that a sufficient (75 mT), but not excessive (150 mT), amount of applied magnetic field strength was best to induce horizontal, rather than angled, lamellar wall alignment in the 350 nm scaffold center. Since a greater percentage of magnetized 350 nm Al_2O_3 particles had greater Γ values (Fig. 4), aggregation and subsequent alignment of those larger particles within lamellar walls should be indicative of more susceptibility to increased magnetic field strength. Lamellar wall alignment was not uniformly horizontal or angled at 75 mT or 150 mT, respectively,

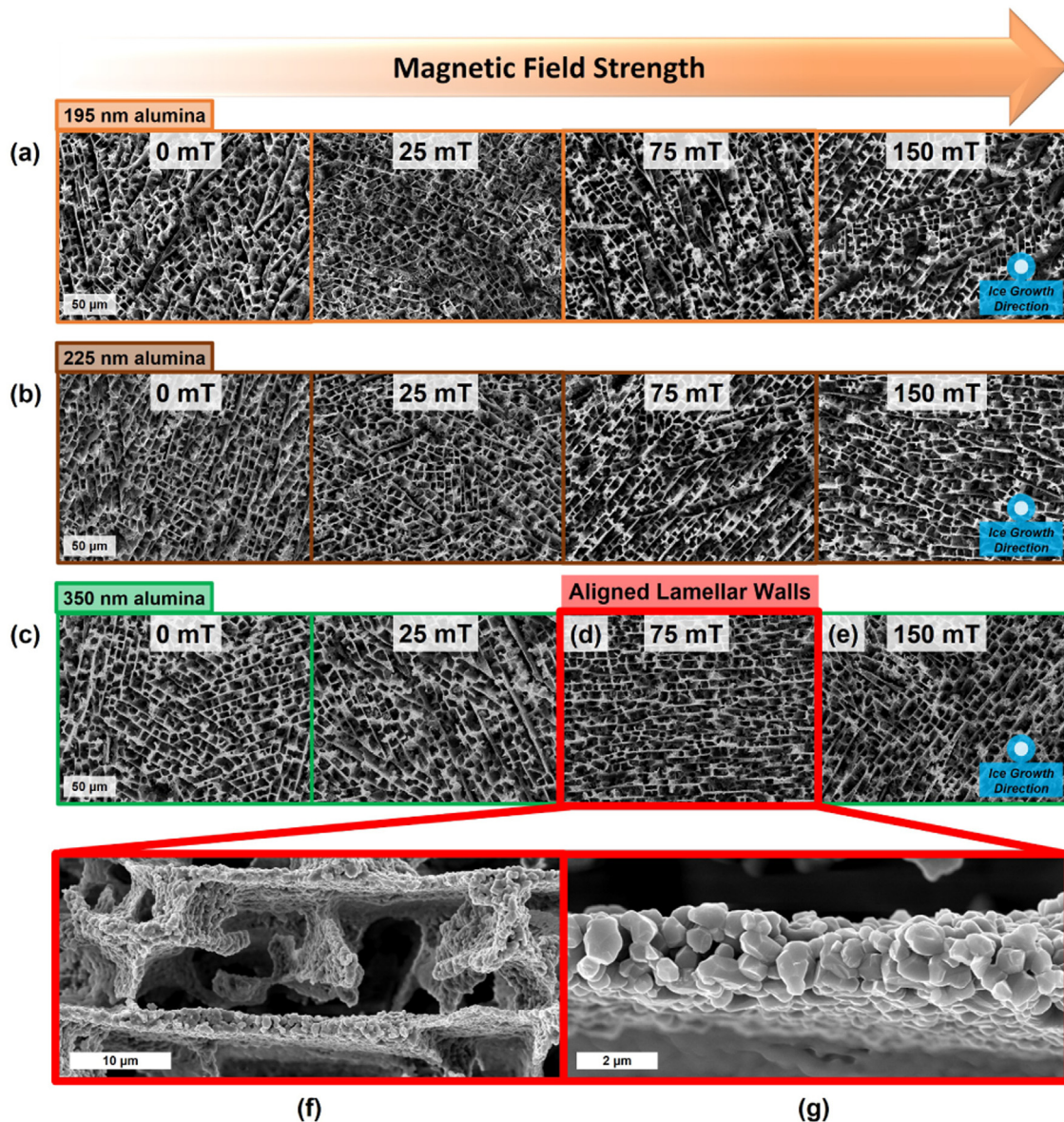


Fig. 5. Scanning electron micrographs of scaffold center regions for different sized magnetized alumina particles after magnetic freeze casting at 0, 25, 75 and 150 mT. (a) 195 nm alumina particles did not exhibit lamellar wall alignment at any of the applied magnetic fields, while (b) 225 nm alumina particles had limited alignment at 150 mT. (c) 350 nm alumina particles had lamellar wall alignment that was most evident at (d) 75 mT, however, at (e) 150 mT there was angled alignment likely due to flux field effects. (f) Closer examination of the scaffold microstructures shows mineral bridge formation and (g) particles sintered together within lamellar walls aligned along the magnetic field axis.

so further reproducibility of these results necessitates more samples or future magnetic freeze casting work with larger magnetized particles to confirm general trends observed in this study.

Different sized Al_2O_3 particles produced scaffolds with similar porosity ($\approx 80\text{--}85\%$, Table 1) and lamellar wall thickness (2.3–3 μm , Table 1) as previous freeze casting work with ZrO_2 [35] and TiO_2 [41] that had the same processing conditions. However, the pore area for the Al_2O_3 scaffolds (35–45 μm^2 , Table 1) was $>20\times$ and $5\times$ smaller than for ZrO_2 [35] and TiO_2 [41] scaffolds, respectively, despite Al_2O_3 particles having similar sizes as ZrO_2 and TiO_2 particles. Molecular dynamic simulations indicate material properties (e.g., surface morphology, hydrophobicity, lattice mismatch) [72] and particle surface modification with adsorbed molecules can significantly increase or decrease ice nucleation rate [73], which can help explain this discrepancy. Increased magnetic field strength (440–560 mT) can have a weak effect on physicochemical properties of water (e.g., surface tension, viscosity) [74–76], however, the lower magnetic field strength (25–150 mT) used in this study was assumed to have not affected ice nucleation or crystal growth.

Freeze casting at a slower cooling ramp (-5 K/min) with a wider range of Al_2O_3 sizes (0.2–3.4 μm), Deville et al. [77] speculated that smaller particles with higher surface area had more ice nucleation sites that led to scaffolds with larger pore area and lamellar wall thickness. For this study, a much narrower Al_2O_3 particle size range (195–350 nm) likely mitigated any large difference between number of nucleation sites, although pore area and lamellar wall thickness slightly increased for larger magnetized Al_2O_3 particles (Table 1). Altered ice nucleation rates in other freeze casting systems using different solidification rates, materials, particle sizes and unmodified surfaces can further complicate comparison of measured scaffold properties. Additional experimental work on heterogeneous ice nucleation is certainly needed to correlate empirical results with fundamental understanding of physicochemical processes from molecular dynamics simulations [72].

Magnetic freeze casting used with slurries of 10 vol% ZrO_2 mixed with 50 nm Fe_3O_4 particles showed mineral bridge alignment and thickness increased as Fe_3O_4 content and transverse magnetic field strength increased [53]. In those slurry mixtures, larger Fe_3O_4 particles with ferromagnetic properties ($\Gamma \gg 1$) led to particle chaining of Fe_3O_4 concentrated within aligned and thickened mineral bridges along the transverse magnetic field axis. In the present study, slight thickening of the lamellar walls occurred at varying magnetic field strength for 350 nm particles only (Table 1) and resulted in mostly uniform microstructures compared with previous work.

3.3. Mechanical properties

Freeze cast scaffold porosity from a slurry of 10 vol% Al_2O_3 was consistent across all samples ($\approx 80\text{--}85\%$), so direct comparison of mechanical properties could be correlated between particle sizes. At no applied magnetic field, pore area and lamellar wall thickness increased with particle size (Table 1). Fig. 6a shows a representative y -axis stress-strain

curve for 350 nm scaffolds prepared with and without an applied magnetic field. The large uneven plateau region on the plot is typical of porous materials, where individual walls are fracturing over a large strain range. It is clear that Young's modulus (E) and ultimate compressive strength (UCS) are larger with an applied magnetic field, corroborating the results of Porter et al. [51] who found the same effect in TiO_2 scaffolds.

Fig. 6b, c summarizes E and UCS in the magnetic field, y -axis, and ice growth, z -axis, directions as a function of particle size and magnetic field strength. In Fig. 6b, E and UCS in the y -axis ranged between $\approx 30\text{--}90\text{ MPa}$ and $\approx 1.2\text{--}2.8\text{ MPa}$, respectively. In general, both E and UCS increased with increasing particle size, which is attributable to scaffolds with larger particles having thicker lamellar walls. For 225 nm scaffolds, E increased by $\approx 50\%$ at 150 mT compared to 0 mT (Fig. 6b), while E did not increase at any magnetic field strength for 195 nm scaffolds. The 350 nm scaffolds prepared at 75 mT had the highest E increase by $\approx 100\%$ compared to 0 mT (Fig. 6b), which correlated with more horizontal lamellar wall alignment observed in SEM micrographs. At 150 mT, magnetic flux lines displayed some curvature from origination at the bar magnet poles and were not parallel throughout the sample, as found in finite element models [53]. Lower E value at 150 mT is attributable to curvature of the magnetic flux in the scaffold center, which caused less horizontal lamellar wall alignment. Overall, particle sizes $< 350\text{ nm}$ show limited or no effect on transverse axis properties when a magnetic field is applied during solidification.

Fig. 6c shows that E and UCS in the z -axis ranged between $\approx 100\text{--}260\text{ MPa}$ and $\approx 10\text{--}21\text{ MPa}$, respectively. Both E and UCS values were much greater in the z -axis than the y -axis because ice templated crystal growth guided formation of aligned lamellar walls along the ice growth direction. In general, both E and UCS increased with particle size in the z -axis, again due to the increase in lamellar wall thickness (Table 1). For 350 nm scaffolds, more so than for scaffolds made up of smaller particles, increased magnetic field strength seemed to induce more aggregation between particles to form broader regions of aligned lamellar walls in “grains” oriented transverse to the freezing direction. Generally, scaffold compression along the z -axis causes crack formation and growth to occur due to local buckling of lamellar walls. However, for 350 nm scaffolds subjected to increased magnetic field strength, the compressive load was distributed more evenly by the ordered lamellar wall “grains” which had mineral bridges between parallel lamellae that prevented Euler buckling by hindering crack propagation [39,41]. In both y and z -axes, E was a more reliable indicator of scaffold strengthening than UCS. Consistent trends for UCS were not evident in the y or z -axes for scaffolds of any particle size at increased magnetic field strength due to variable defects that can have a large impact during mechanical compression.

Previous work demonstrated enhancement of E and UCS due to lamellar wall alignment along the y -axis for a slurry mixture of TiO_2 mixed with ferromagnetic Fe_3O_4 ($\approx 50\text{ nm}$) at an applied magnetic field of 120 mT [51]. Similar improvement in the y -axis was evident for ZrO_2 and Fe_3O_4 at 90 mT, although mineral bridges were aligned rather than the lamellar walls [53]. The amount of magnetic material

Table 1

Porosity, pore area and lamellar wall thickness of alumina particle scaffolds freeze cast at various static magnetic fields (0, 75, 150 mT). Sample size for each condition: $N = 6$. All data reported are mean \pm standard error (standard deviation / \sqrt{N}).

	Magnetic field strength (mT)	195 nm particles	225 nm particles	350 nm particles
Porosity (%)	0	83.74 \pm 0.15	83.35 \pm 0.17	82.60 \pm 0.19
	75	84.77 \pm 0.29	83.44 \pm 0.18	82.33 \pm 0.18
	150	85.29 \pm 0.11	81.60 \pm 0.33	81.83 \pm 0.58
Pore area (μm^2)	0	37.28 \pm 2.57	41.20 \pm 2.56	43.33 \pm 2.92
	75	37.82 \pm 2.38	38.12 \pm 2.17	47.29 \pm 3.50
	150	34.64 \pm 2.21	41.97 \pm 2.69	42.54 \pm 2.53
Lamellar wall thickness (μm)	0	2.32 \pm 0.05	2.53 \pm 0.06	2.85 \pm 0.07
	75	2.31 \pm 0.07	2.58 \pm 0.07	2.91 \pm 0.08
	150	2.34 \pm 0.09	2.56 \pm 0.08	3.04 \pm 0.08

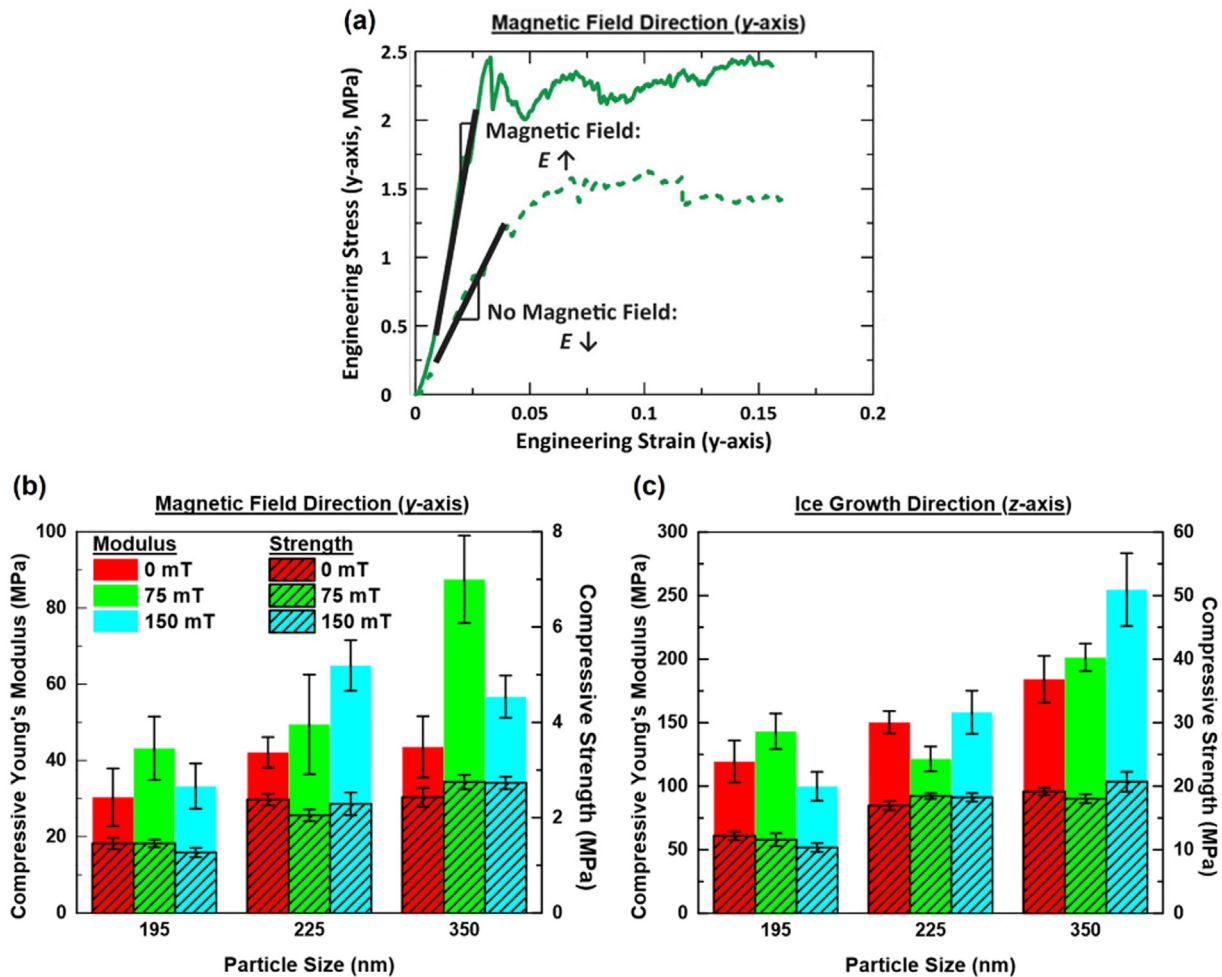


Fig. 6. Comparison of compressive mechanical properties with stress–strain curve, modulus and strength values for porous scaffolds of magnetized alumina particles prepared by magnetic freeze casting. (a) A representative stress–strain curve for 350 nm particles made with no magnetic field (dotted line) and static magnetic field of 75 mT (solid line). Compressive Young's modulus and ultimate strength as a function of particle size and magnetic field strength in the (b) magnetic field (y-axis) and (c) ice growth direction (z-axis). Data points are the mean of $N = 6$ measurements with error bars representing \pm standard error (standard deviation / \sqrt{N}).

added to those TiO_2 and ZrO_2 slurries (up to 9 wt% Fe_3O_4 particles) may have contributed to enhanced UCS values in the y-axis, which may help explain why similar trends were not observed in this work. From this

work, surface magnetized Al_2O_3 particles subjected to a sufficient magnetic field produced observable lamellar wall alignment in the scaffold center at 75 mT for 350 nm scaffolds and 150 mT for 225 nm scaffolds.

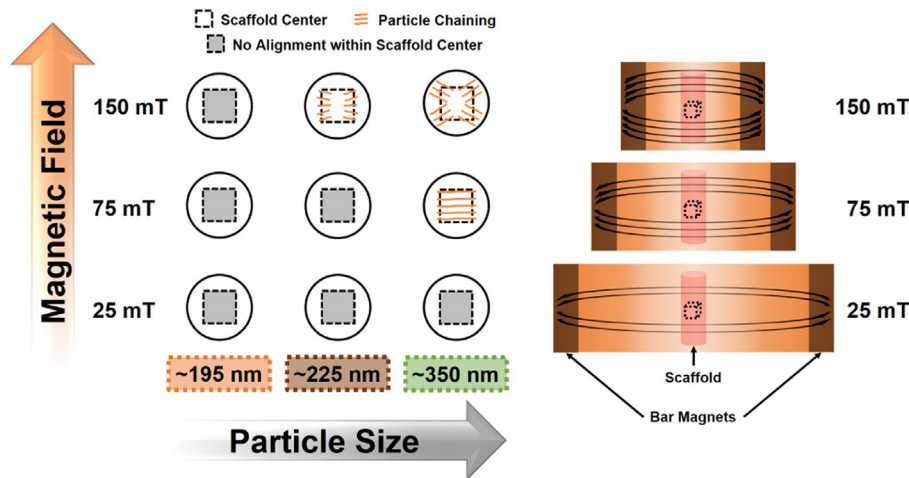


Fig. 7. Lamellar wall alignment within the scaffold center as a function of magnetic field strength and magnetized particle size. The schematic indicates the extent of particle chaining (orange line) leading to lamellar wall alignment in the scaffold center (dotted box) for each magnetized alumina particle size at varying magnetic field strength. Lower magnetic field strength produced no lamellar wall alignment within the scaffold center for smaller particles (dotted gray box). A greater degree of particle chaining for larger particles led to more lamellar wall alignment, although a stronger magnetic field caused that alignment to be angled near the magnet poles instead of along the horizontal axis within the scaffold center.

The extent of interaction energy between magnetized particles needed to induce lamellar wall alignment depended on particle size, thermodynamic variables (temperature, volume fraction) that affect aggregation and time evolution for chain formation before ice nucleation during freeze casting [60,61,63]. Exploration of these three factors will continue with further magnetic freeze casting experimental work.

The schematic diagrams in Fig. 7 summarize how particle chaining (orange lines) can lead to lamellar wall alignment in the scaffold center (dotted box), or not (dotted gray box), for each magnetized particle size at varying magnetic field strengths. For 225 nm particles, greater magnetic field strength (150 mT) led to more interaction energy between particles that overcame thermal agitation force within the slurry and partially aligned lamellar walls within the scaffold center. For 350 nm particles with greater Γ than 195 or 225 nm particles (Fig. 4), more horizontal lamellar wall alignment occurred along the y -axis in the scaffold center at 75 mT compared with too strong of a magnetic field (150 mT) that produced angled lamellar wall alignment.

4. Conclusions

Freeze casting was carried out for the first time with varying surface magnetized alumina (Al_2O_3) particle sizes (195, 225 and 350 nm) and magnetic fields (0, 75 and 150 mT) applied transverse to the ice growth direction. This new method provides an avenue for examination of physical processes that affected particle aggregation leading to lamellar wall alignment in sintered porous scaffolds. Particle size measurement by the dynamic light scattering (DLS) technique combined with magnetometer data indicated larger magnetized particles had greater interaction energy that could lead to more lamellar wall alignment. Scanning electron microscopy characterization of the sintered scaffold center indicated the most horizontal lamellar wall alignment for 350 nm particles at 75 mT, while both compressive Young's modulus ($\approx 100\%$) and strength ($\approx 20\%$) also increased in the magnetic field direction. Scaffolds made of larger particles produced more horizontal lamellar wall alignment at weaker magnetic field strength with thicker lamellar walls that increased Young's modulus and strength. Previous magnetic freeze casting work that used a heterogeneous slurry of magnetite particles mixed with oxide ceramic particles to align lamellar walls and mineral bridges can be extended with this work to include any surface magnetized materials.

Acknowledgements

This work is supported by a Multi-University Research Initiative (MURI) through the Air Force Office of Scientific Research of the United States (AFOSR-FA9550-15-1-0009) and a National Science Foundation Biomaterials Program Grant 1507169. The authors wish to acknowledge students who assisted with magnetic freeze casting and mechanical testing at University of California, San Diego (Khalid Niles-Rodney, Kerry Chou, Christopher Yu, Ming Chengmingjt, Alejandro Valdivia, Angelica Esparza). We thank Prof. Eric Fullerton, Prof. Vitaliy Lomakin and Sohini Manna (University of California, San Diego) for insightful discussions on magnetic properties, Prof. Marc A. Meyers (University of California, San Diego) for assistance with mechanical characterization, Ryan Anderson (University of California, San Diego) for SEM micrographs of magnetized particles and Dr. Jordi Farauo (Institut de Ciencia de Materials de Barcelona), Prof. Albert P. Philipse and Ping Liu (Utrecht University, The Netherlands) for explaining fundamental details about the magnetic coupling parameter equation.

Appendix A. Supplementary data

Supplementary data to this article can be found online at <http://dx.doi.org/10.1016/j.msec.2017.03.246>.

References

- J.L. Kirschvink, J.L. Gould, Biogenic magnetite as a basis for magnetic-field detection in animals, *Biosystems* 13 (3) (1981) 181–201.
- A.J. Kalmijn, I.F. Gonzalez, M.C. McClune, The physical nature of life, *Journal of Physiology-Paris* 96 (5–6) (2002) 355–362.
- C. Walcott, R.P. Green, Orientation of homing pigeons altered by a change in direction of an applied magnetic-field, *Science* 184 (4133) (1974) 180–182.
- J.L. Gould, J.L. Kirschvink, K.S. Deffeyes, Bees have magnetic remanence, *Science* 201 (4360) (1978) 1026–1028.
- J.L. Kirschvink, A. Kobayashikirschvink, B.J. Woodford, Magnetite biomineralization in the human brain, *Proc. Natl. Acad. Sci. U. S. A.* 89 (16) (1992) 7683–7687.
- R. Blakemore, Magnetotactic bacteria, *Science* 190 (4212) (1975) 377–379.
- K. Inoue, K. Sassa, Y. Yokogawa, Y. Sakka, M. Okido, S. Asai, Control of crystal orientation of hydroxyapatite by imposition of a high magnetic field, *Mater. Trans.* 44 (6) (2003) 1133–1137.
- S.H. Lee, L. Feng, J. Yin, J.S. Lee, X. Zhu, T.S. Suzuki, Y. Sakka, H. Tanaka, Dense SiC containing strongly aligned plate-like grains by magnetic treatment, *Ceram. Int.* 41 (3) (2015) 5079–5084.
- M. Ozen, M. Mertens, F. Snijders, G. Van Tendeloo, P. Cool, Texturing of hydrothermally synthesized BaTiO_3 in a strong magnetic field by slip casting, *Ceram. Int.* 42 (4) (2016) 5382–5390.
- Y. Sakka, T.S. Suzuki, Textured development of feeble magnetic ceramics by colloidal processing under high magnetic field, *J. Ceram. Soc. Jpn.* 113 (1313) (2005) 26–36.
- T.S. Suzuki, Y. Sakka, Fabrication of textured titania by slip casting in a high magnetic field followed by heating, *Jpn. J. Appl. Phys. Part 2 - Lett.* 41 (11A) (2002) L1272–L1274.
- T.S. Suzuki, Y. Sakka, Control of texture in ZnO by slip casting in a strong magnetic field and heating, *Chem. Lett.* 31 (12) (2002) 1204–1205.
- T.S. Suzuki, T. Uchikoshi, Y. Sakka, Control of texture in alumina by colloidal processing in a strong magnetic field, *Sci. Technol. Adv. Mater.* 7 (4) (2006) 356–364.
- D. Vriami, E. Beaugnon, J.P. Erauw, J. Vleugels, O. Van der Biest, Texturing of 3Y-TZP zirconia by slip casting in a high magnetic field of 17.4T, *J. Eur. Ceram. Soc.* 35 (14) (2015) 3959–3967.
- Z.G. Yang, J.B. Yu, C.J. Li, Y.B. Zhong, W.D. Xuan, Z.M. Ren, Q.L. Wang, Y.M. Dai, H. Wang, Preparation of textured porous Al_2O_3 ceramics by slip casting in a strong magnetic field and its mechanical properties, *Cryst. Res. Technol.* 50 (8) (2015) 645–653.
- H. Le Ferrand, F. Bouville, T.P. Niebel, A.R. Studart, Magnetically assisted slip casting of bioinspired heterogeneous composites, *Nat. Mater.* 14 (11) (2015) 1172.
- R.M. Erb, R. Libanori, N. Rothfuchs, A.R. Studart, Composites reinforced in three dimensions by using low magnetic fields, *Science* 335 (6065) (2012) 199–204.
- R.M. Erb, K.H. Cherenack, R.E. Stahel, R. Libanori, T. Kinkeldei, N. Munzenrieder, G. Troster, A.R. Studart, Locally reinforced polymer-based composites for elastic electronics, *ACS Appl. Mater. Interfaces* 4 (6) (2012) 2860–2864.
- R. Libanori, R.M. Erb, A.R. Studart, Mechanics of platelet-reinforced composites assembled using mechanical and magnetic stimuli, *ACS Appl. Mater. Interfaces* 5 (21) (2013) 10794–10805.
- D. Carnelli, R. Libanori, B. Feichtenschlager, L. Nicoleau, G. Albrecht, A.R. Studart, Cement-based composites reinforced with localized and magnetically oriented Al_2O_3 microplatelets, *Cem. Concr. Res.* 78 (2015) 245–251.
- R.M. Erb, J.S. Sander, R. Grisch, A.R. Studart, Self-shaping composites with programmable bioinspired microstructures, *Nat. Commun.* 4 (2013) 1712.
- R. Libanori, F.B. Reusch, R.M. Erb, A.R. Studart, Ultrahigh magnetically responsive microplatelets with tunable fluorescence emission, *Langmuir* 29 (47) (2013) 14674–14680.
- D. Kokkinis, M. Schaffner, A.R. Studart, Multimaterial magnetically assisted 3D printing of composite materials, *Nat. Commun.* 6 (2015) 10.
- J.J. Martin, B.E. Fiore, R.M. Erb, Designing bioinspired composite reinforcement architectures via 3D magnetic printing, *Nat. Commun.* 6 (2015) 7.
- U.G.K. Wegst, H. Bai, E. Saiz, A.P. Tomsia, R.O. Ritchie, Bioinspired structural materials, *Nat. Mater.* 14 (1) (2015) 23–36.
- S. Weiner, H.D. Wagner, The material bone: structure mechanical function relations, *Annu. Rev. Mater. Sci.* 28 (1998) 271–298.
- M.E. Launey, M.J. Buehler, R.O. Ritchie, On the mechanistic origins of toughness in bone, in: D.R. Clarke, M. Ruhle, F. Zok (Eds.), *Annual Review of Materials Research*, Annual Reviews, Vol. 40, 2010, pp. 25–53 Palo Alto.
- R.M.V. Pidaparti, C.H. Turner, Cancellous bone architecture: advantages of nonorthogonal trabecular alignment under multidirectional joint loading, *J. Biomech.* 30 (9) (1997) 979–983.
- H.F. Zhang, I. Hussain, M. Brust, M.F. Butler, S.P. Rannard, A.I. Cooper, Aligned two- and three-dimensional structures by directional freezing of polymers and nanoparticles, *Nat. Mater.* 4 (10) (2005) 787–793.
- S. Deville, E. Saiz, R.K. Nalla, A.P. Tomsia, Freezing as a path to build complex composites, *Science* 311 (5760) (2006) 515–518.
- E. Munch, M.E. Launey, D.H. Alsem, E. Saiz, A.P. Tomsia, R.O. Ritchie, Tough, bio-inspired hybrid materials, *Science* 322 (5907) (2008) 1516–1520.
- U.G. Wegst, M. Schecter, A.E. Donius, P.M. Hunger, Biomaterials by freeze casting, *Phil. Trans. R. Soc. A* 368 (1917) (2010) 2099–2121.
- P.M. Hunger, A.E. Donius, U.G. Wegst, Platelets self-assemble into porous nacre during freeze casting, *J. Mech. Behav. Biomed. Mater.* 19 (2013) 87–93.
- P.M. Hunger, A.E. Donius, U.G. Wegst, Structure-property-processing correlations in freeze-cast composite scaffolds, *Acta Biomater.* 9 (5) (2013) 6338–6348.
- S.E. Naleway, K.C. Fickas, Y.N. Maker, M.A. Meyers, J. McKittrick, Reproducibility of ZrO_2 -based freeze casting for biomaterials, *Materials Science & Engineering C-Materials for Biological Applications* 61 (2016) 105–112.

- [36] K. Araki, J.W. Halloran, Porous ceramic bodies with interconnected pore channels by a novel freeze casting technique, *J. Am. Ceram. Soc.* 88 (5) (2005) 1108–1114.
- [37] K. Araki, J.W. Halloran, Room-temperature freeze casting for ceramics with non-aqueous sublimable vehicles in the naphthalene-camphor eutectic system, *J. Am. Ceram. Soc.* 87 (11) (2004) 2014–2019.
- [38] R. Guo, C.-A. Wang, A. Yang, Piezoelectric properties of the 1–3 type porous lead zirconate titanate ceramics, *J. Am. Ceram. Soc.* 94 (6) (2011) 1794–1799.
- [39] E. Munch, E. Saiz, A.P. Tomsia, S. Deville, Architectural control of freeze-cast ceramics through additives and Templating, *J. Am. Ceram. Soc.* 92 (7) (2009) 1534–1539.
- [40] M.M. Porter, J. McKittrick, M.A. Meyers, Biomimetic materials by freeze casting, *JOM* 65 (6) (2013) 720–727.
- [41] M.M. Porter, R. Imperio, M. Wen, M.A. Meyers, J. McKittrick, Bioinspired scaffolds with varying pore architectures and mechanical properties, *Adv. Funct. Mater.* 24 (14) (2014) 1978–1987.
- [42] S.E. Naleway, C.F. Yu, M.M. Porter, A. Sengupta, P.M. Iovine, M.A. Meyers, J. McKittrick, Bioinspired composites from freeze casting with clathrate hydrates, *Mater. Des.* 71 (2015) 62–67.
- [43] Y.F. Tang, S. Qiu, C. Wu, Q. Miao, K. Zhao, Freeze cast fabrication of porous ceramics using tert-butyl alcohol-water crystals as template, *J. Eur. Ceram. Soc.* 36 (6) (2016) 1513–1518.
- [44] C. Tallon, R. Moreno, M.I. Nieto, Shaping of porous alumina bodies by freeze casting, *Adv. Appl. Ceram.* 108 (5) (2009) 307–313.
- [45] Y.M. Tan, O. Cervantes, S. Nam, J.D. Molitoris, J.P. Hooper, Dynamic fragmentation of cellular, ice-templated alumina scaffolds, *J. Appl. Phys.* 119 (2) (2016) 8.
- [46] S.M. Miller, X. Xiao, K.T. Faber, Freeze-cast alumina pore networks: effects of freezing conditions and dispersion medium, *J. Eur. Ceram. Soc.* 35 (13) (2015) 3595–3605.
- [47] F. Bouville, E. Portuguez, Y.F. Chang, G.L. Messing, A.J. Stevenson, E. Maire, L. Courtois, S. Deville, Templated grain growth in macroporous materials, *J. Am. Ceram. Soc.* 97 (6) (2014) 1736–1742.
- [48] F. Bouville, E. Maire, S. Meille, B. Van de Moortele, A.J. Stevenson, S. Deville, Strong, tough and stiff bioinspired ceramics from brittle constituents, *Nat. Mater.* 13 (5) (2014) 508–514.
- [49] H. Bai, Y. Chen, B. Delattre, A.P. Tomsia, R.O. Ritchie, Bioinspired large-scale aligned porous materials assembled with dual temperature gradients, *Sci. Adv.* 1 (11) (2015), e1500849.
- [50] H. Bai, F. Walsh, B. Gludovatz, B. Delattre, C.L. Huang, Y. Chen, A.P. Tomsia, R.O. Ritchie, Bioinspired hydroxyapatite/poly(methyl methacrylate) composite with a nacre-mimetic architecture by a bidirectional freezing method, *Adv. Mater.* 28 (1) (2016) 50.
- [51] M.M. Porter, M. Yeh, J. Strawson, T. Goehring, S. Lujan, P. Siripapaporn, M.A. Meyers, J. McKittrick, Magnetic freeze casting inspired by nature, *Mater. Sci. Eng. A-Struct. Mater. Prop. Microstruct. Process.* 556 (2012) 741–750.
- [52] M.M. Porter, L. Meraz, A. Calderon, H.J. Choi, A. Chouhan, L. Wang, M.A. Meyers, J. McKittrick, Torsional properties of helix-reinforced composites fabricated by magnetic freeze casting, *Compos. Struct.* 119 (2015) 174–184.
- [53] M.M. Porter, P. Niksiar, J. McKittrick, Microstructural control of colloidal-based ceramics by directional solidification under weak magnetic fields, *J. Am. Ceram. Soc.* 99 (6) (2016) 1917–1926.
- [54] A.H. Lu, E.L. Salabas, F. Schuth, Magnetic nanoparticles: synthesis, protection, functionalization, and application, *Angew. Chem. Int. Ed. Eng.* 46 (8) (2007) 1222–1244.
- [55] A.A. Neurauter, M. Bonyhadi, E. Lien, L. Nokleby, E. Ruud, S. Camacho, T. Aarvak, Cell isolation and expansion using Dynabeads((R)), in: A. Kumar, I.Y. Galaev, B. Mattiasson (Eds.), *Cell Separation: Fundamentals, Analytical and Preparative Methods*, Springer-Verlag, Berlin 2007, pp. 41–73.
- [56] M.R. McPhail, J.A. Sells, Z. He, C.C. Chusei, Charging nanowalls: adjusting the carbon nanotube isoelectric point via surface functionalization, *J. Phys. Chem. C* 113 (2009) 14102–14109.
- [57] G.E. Brown, V. Henrich, W. Casey, D. Clark, C. Eggleston, A. Felmy, D.W. Goodman, M. Grätzel, G. Maciel, M.I. McCarthy, K.H. Nealson, D.A. Sverjensky, M.F. Toney, J.M. Zachara, Review: metal oxide surfaces and their interactions with aqueous solutions and microbial organisms, *Chem. Rev.* 99 (1999) 77–174.
- [58] M. Kosmulski, pH-dependent surface charging and points of zero charge. IV. Update and new approach, *J. Colloid Interface Sci.* 337 (2) (2009) 439–448.
- [59] A.P. Philipse, D. Maas, Magnetic colloids from magnetotactic bacteria: chain formation and colloidal stability, *Langmuir* 18 (25) (2002) 9977–9984.
- [60] J.S. Andreu, J. Camacho, J. Faraudo, Aggregation of superparamagnetic colloids in magnetic fields: the quest for the equilibrium state, *Soft Matter* 7 (6) (2011) 2336–2339.
- [61] J. Faraudo, J.S. Andreu, J. Camacho, Understanding diluted dispersions of superparamagnetic particles under strong magnetic fields: a review of concepts, theory and simulations, *Soft Matter* 9 (29) (2013) 6654–6664.
- [62] P. Liu, J.W.J. de Folter, A.V. Petukhov, A.P. Philipse, Reconfigurable assembly of superparamagnetic colloids confined in thermo-reversible microtubes, *Soft Matter* 11 (31) (2015) 6201–6211.
- [63] J. Faraudo, J.S. Andreu, C. Calero, J. Camacho, Predicting the self-assembly of superparamagnetic colloids under magnetic fields, *Adv. Funct. Mater.* 26 (22) (2016) 3837–3858.
- [64] A.R. Studart, Biologically inspired dynamic material systems, *Angewandte Chemie-International Edition* 54 (11) (2015) 3400–3416.
- [65] D. Ghosh, M. Banda, H. Kang, N. Dhavale, Platelets-induced stiffening and strengthening of ice-templated highly porous alumina scaffolds, *Scr. Mater.* 125 (2016) 29–33.
- [66] O.A. Graeve, A. Madadi, R. Kanakala, K. Sinha, Analysis of particle and crystallite size in tungsten nanopowder synthesis, *Metall. Mater. Trans. A* 41 (10) (2010) 2691–2697.
- [67] O.A. Graeve, H. Fathi, J.P. Kelly, M.S. Saterlie, K. Sinha, G. Rojas-George, R. Kanakala, D.R. Brown, E.A. Lopez, Reverse micelle synthesis of oxide nanopowders: mechanisms of precipitate formation and agglomeration effects, *J. Colloid Interface Sci.* 407 (2013) 302–309.
- [68] C.I. Vargas-Consuelos, K. Seo, M. Camacho-Lopez, O.A. Graeve, Correlation between particle size and Raman vibrations in WO₃ powders, *J. Phys. Chem. C* 118 (18) (2014) 531–537.
- [69] T.M. Nocera, J. Chen, C.B. Murray, G. Agarwal, Magnetic anisotropy considerations in magnetic force microscopy studies of single superparamagnetic nanoparticles, *Nanotechnology* 23 (49) (2012) 495704.
- [70] D.X. Chen, A. Sanchez, E. Taboada, A. Roig, N. Sun, H.C. Gu, Size determination of superparamagnetic nanoparticles from magnetization curve, *J. Appl. Phys.* 105 (8) (2009) 6.
- [71] H. Wang, Q.W. Chen, L.X. Sun, H.P. Qi, X. Yang, S. Zhou, J. Xiong, Magnetic-field-induced formation of one-dimensional magnetite nanochains, *Langmuir* 25 (12) (2009) 7135–7139.
- [72] M. Fitzner, G.C. Sosso, S.J. Cox, A. Michaelides, The many faces of heterogeneous ice nucleation: interplay between surface morphology and hydrophobicity, *J. Am. Chem. Soc.* 137 (42) (2015) 13658–13669.
- [73] S.J. Cox, S.M. Kathmann, B. Slater, A. Michaelides, Molecular simulations of heterogeneous ice nucleation. I. Controlling ice nucleation through surface hydrophilicity, *J. Chem. Phys.* 142 (18) (2015) 5.
- [74] K. Higashitani, K. Okuhara, S. Hatade, Effects of magnetic fields on stability of non-magnetic ultrafine colloidal particles, *J. Colloid Interface Sci.* 152 (1) (1992) 125–131.
- [75] X.-F. Pang, B. Deng, The changes of macroscopic features and microscopic structures of water under influence of magnetic field, *Phys. B Condens. Matter* 403 (19–20) (2008) 3571–3577.
- [76] R. Cai, H. Yang, J. He, W. Zhu, The effects of magnetic fields on water molecular hydrogen bonds, *J. Mol. Struct.* 938 (1–3) (2009) 15–19.
- [77] S. Deville, E. Maire, A. Lasalle, A. Bogner, C. Gauthier, J. Leloup, C. Guizard, Influence of particle size on ice nucleation and growth during the ice-templating process, *J. Am. Ceram. Soc.* 93 (9) (2010) 2507–2510.